Impregnation of Fe^{3+} into MCM-41 Pores: Effect of Fe^{3+} Concentration on the Weight Percent of Fe-Frameworks and Fe-Non-Frameworks

Suyanta Suyanta*, Agus Kuncaka, and Mudasir Mudasir

Department of Chemistry, Faculty of Mathematics and Natural Sciences, Universitas Gadjah Mada, Sekip Utara, Yogyakarta 55281, Indonesia

* ***Corresponding author:***

email: suyanta_mipa@ugm.ac.id

Received: November 28, 2022
Accepted: May 15, 2023

DOI: 10.22146/ijc.79468

Abstract: *Silica from rice husks (RH) has been used as a starting ingredient in the sonication synthesis of MCM-41 (RH-MCM-41). The impregnation of Fe^{3+} into RH-MCM-41 pores to produce RH-MCM-41 containing Fe_2O_3 and Fe (denoted as Fe_2O_3-Fe-RH-MCM-41) was carried out by examining the effect of various Fe^{3+} concentrations on the weight percent of Fe-frameworks (Fe^{3+} that replaces Si^{4+} in silicate frameworks) and Fe-non-frameworks, i.e., the iron oxide formed outside the silicate frameworks. Fe_2O_3-Fe-RH-MCM-41 was washed with a 0.01 M HCl solution to remove Fe-non-frameworks from the materials and give Fe-RH-MCM-41 containing Fe-frameworks. The Fe content in Fe_2O_3-Fe-RH-MCM-41 (Fe-total) and Fe-RH-MCM-41 (Fe-frameworks) for each sample was determined by an AAS (atomic absorption spectrometer), whereas the content of Fe-non-frameworks was calculated from the difference between Fe-total and Fe-frameworks. The XRD (X-ray diffraction) pattern, N_2 adsorption-desorption isotherm profile, as well as the TEM (transmission electron microscope) image clearly demonstrate that the RH-MCM-41 exhibits an ordered p6mm hexagonal mesostructure with a large specific surface area and uniform pore size. Based on the weight percents of Fe-frameworks found in each sample, it is clear that the content of Fe-non-frameworks is significantly enhanced compared to that of Fe-frameworks when the more concentrated Fe^{3+} is used.*

Keywords: *RH-MCM-41; impregnation; Fe-frameworks; Fe-non-frameworks*

■ INTRODUCTION

Zeolites are being used as solid acid catalysts in a growing number of refining processes, as well as in the production of petrochemicals and specialty chemicals, because of their remarkable environmental friendliness, shape selectivity, durability, and reusability [1-2]. However, this material cannot be used to catalyze processes involving big molecules due to its very tiny (± 1 nm) pore size [3]. Thankfully, the mesoporous M41S family, which was discovered in 1992, has numerous advantages over microporous materials because of its larger pore size (3-10 nm) [4].

In general, silica precursors such as tetraethyl orthosilicate (TEOS) [5-7] and sodium silicate [8-11] are used in the synthesis of MCM-41, which is relatively expensive. Iron ore tailing [12-13], siliceous sugar industry waste [14], silicon carbide sludge and granite sludge [15], bentonite [16] and rice husk ash [17-19] have all been investigated for use as a silica precursor in the manufacture of MCM-41 to minimize production costs. Rice husk ash (RH) is the most potent natural substance because it contains SiO_2 at concentrations of over 90% [20-22]. Rice is also widely grown in China, India, Pakistan, and East Asia [23]. Rice Husk-MCM-41 (RH-MCM-41) prepared from rice husk material is reported to possess some properties such as porosity, crystallinity, and hydrothermal stability that are comparable to those synthesized from commercial silicates, such as tetraethyl orthosilicate (TEOS) [24].

MCM-41 is usually produced via the hydrothermal process, which entails heating the reactants with air in a sealed container (autoclave) [25-27]. Since the hydrothermal method requires a lot of time and energy to complete the reaction, it is less efficient and does not

meet the green chemistry principle. Alternative approaches, such as the sonochemistry process, which makes use of ultrasonic waves, have been used in a number of works to synthesize MCM-41 [28-30]. Ultrasonic vibrations can initiate chemical reactions in liquids by producing tiny bubbles known as micro-cavitation. The high temperature and pressure created by the pulsation of the bubbles [31], of course, create conditions conducive for chemical reactions to occur. The sonochemistry approach requires less time and energy, making it a more cost-effective and environmentally friendly technique.

It is well known that pure siliceous Si-MCM-41 has no acidity and lacks intrinsic catalytic applicability. Therefore, it must be heterogenized with transition metals to make it suitable for catalytic applications [32]. For example, Fe has been added to the MCM-41 structure to yield Fe-MCM-41, which has a negative framework charge due to some replacement of SiO_4 by FeO_4 tetrahedrons. Counter ions, such as H^+, could balance out the internal negative charge of the structure to produce the Brønsted-acidity [33]. For this reason, iron-modified mesoporous MCM-41 silica materials, Fe-MCM-41, have received significant attention as new nanostructured and catalyst materials in the last decade [34].

So far, impregnation has become one of several approaches to incorporate transition metals into the mesoporous MCM-41 frameworks [35-38]. However, in the impregnation of Fe^{3+} into MCM-41 material, there is always evidence for isomorphic substitution of trivalent iron in the frameworks that lead to the formation of Fe-MCM-41, as well as iron oxide nanoparticles on the outer frameworks [38]. In general, transition metal oxides also have catalytic properties, so several researchers have synthesized metal oxide nanoparticles in the pores of MCM-41 [39-40] and SBA-15 [41-42], which are applied as catalysts for various reactions. In contrast, there are also some serious problems if the filling of the pores by Fe_2O_3 nanoparticles (denoted as Fe-non-frameworks) induces the blockage of the trivalent iron in the frameworks (denoted as Fe-frameworks), thereby reducing the catalytic activity as reported by Pieterse et al. [43]. Significant blockage of the pore channels apparently reduces the diffusion of the reactants. It means that the iron oxide nanoparticles outside frameworks are not preferable if their content exceeds the appropriate level. Therefore, the optimum ratio of Fe-frameworks to Fe-non-frameworks contents should be investigated to maximize the catalytic activity of the materials.

As far as we know, there are hardly any reports that focus on the investigation of the ratio of Fe-frameworks to Fe-non-frameworks in MCM-41. In fact, this information is essentially required in designing catalysts with the best performance in their catalytic activity. Based on this idea, in this study, we have synthesized MCM-41 from rice husk ash (RH-MCM-41) by the sonication method and systematically investigated the effect of Fe^{3+} impregnation at various concentrations on the weight percent ratio of Fe-frameworks to Fe-non-frameworks in the RH-MCM-41 with the purpose of maximizing the catalytic properties of the materials. The use of rice husk as starting material is very advantageous, as there is a lot of rice husk waste in our surroundings, while the choice of the sonication method reduces the energy used for heating; thus, this study meets the principle of green chemistry and is environmentally more benign.

■ EXPERIMENTAL SECTION

Materials

The materials used in this study were rice husk taken from the rice huller in the district of Bantul, Special Region of Yogyakarta, Indonesia. Merck (Germany) provided the chemicals used in this study, which included hydrochloric acid (HCl, 37%), cetyltrimethylammonium bromide (CTAB, 99%), sulfuric acid (H_2SO_4, 96%), sodium hydroxide (NaOH, 100%), ferric nitrate nonahydrate ($Fe(NO_3)_3{\cdot}9H_2O$, pro analysis), and nitric acid (HNO_3, 65%). All of these chemicals are of analytical grade and are used directly without pretreatment. All experiments utilized distilled water.

Instrumentation

The instrumentations used in this study were ultrasonic waves produced by the Bransonic 220

ultrasonic device at room temperature (25 to 32 °C) using a 48 kHz frequency and a 100 W heating capacity. On a Shimadzu model XD-3H X-ray diffractometer operating at room temperature, X-ray diffraction (XRD) patterns were produced using Cu-K_α powder that had been irradiated at = 0.154 nm. A Shimadzu FTIR-8010PC was used to carry out the Fourier-transform infrared (FTIR) spectroscopy examination. The KBr disc technique was used to get the spectra at room temperature and the transmittance mode in the 4000–400 cm^{-1} range. Using the Quantachrome Nova 1200 gas sorption analyzer, we looked at the nitrogen adsorption-desorption isotherm at the temperature of liquid nitrogen (GSA). Prior to the examination, samples were outgassed for a whole night at 250 °C. The Brunauer-Emmett-Teller (BET) surface area is determined by the multipoint BET method using adsorption data at relative pressures (P/P_0) between 0.03 and 0.1. At a relative pressure of 0.95, a mesoporous volume was calculated using isotherms. The Barrett-Joyner-Halenda (BJH) approach was used to calculate the average mesoporous diameter based on the nitrogen isotherm adsorption branch. The transmission electron microscope (TEM, JEM-3010) was used to analyze the properties of the RH-MCM-41 pores. The Atomic Absorption Spectrophotometer (AAS, Perkin Elmer 3110) was used to determine the content of Fe in the samples.

Procedure

The extraction of silica and synthesis of sodium silicate solution

The following procedure, similar to the one we previously reported [25], was used to obtain rice husk silica. First, rice husks were washed using water and dried for 12 h at 120 °C. The clean and dry rice husks (100 g) were put into a 3 M HCl solution (500 mL) and then refluxed at 80 °C for 3 h in a round-bottom flask equipped with a magnetic stirrer. The mixture was cooled, filtered, and washed with distilled water to remove residual acid. The result was again dried at a temperature of 120 °C for 12 h, then calcined at a temperature of 650 °C for 6 h at a speed of 2 °C min^{-1}. To make sodium silicate solution, rice husk silica (4.0 g) and NaOH pellets (1.25 g) were put into distilled water (35 g), then stirred to form a gel. This gel was heated to 80 °C with stirring for 2 h, then cooled in the air to room temperature.

Synthesis of RH-MCM-41

To produce a CTAB solution, CTAB (10 g) was added to distilled water (50 mL) at 60 °C and stirred for 30 min. A 15-mL solution of sodium silicate was added to the above CTAB solution to form the gel. The pH of this gel was adjusted to 11 by steadily dropping 5 M H_2SO_4. After that, the gel was placed in a sealed glass bottle and exposed to ultrasonic exposure at a frequency of 40 Hz at room temperature for 180 min. The white precipitate was collected after the ultrasonic treatment, rinsed with the necessary amount of distilled water, and dried at 110 °C for 100 min. The sample was calcined in air at a rate of 2 °C min^{-1} to 540 °C and held there for 5 h for the template to dissipate, and RH-MCM-41 was produced.

Impregnation of Fe^{3+} into RH-MCM-41 pores

Initially, RH-MCM-41 (1 g) was activated by heating at 120 °C for 3 h. The sample was then placed in a 100 mL solution of various concentrations (0.02, 0.04, 0.06, 0.08, and 0.10 M) of $Fe(NO_3)_3{\cdot}9H_2O$ solutions that had been acidified with HNO_3 until pH 2. At 40 °C, the mixture was magnetically stirred for 8 h, then left to stand for 4 h to achieve maximal impregnation. The solid phase was filtered out with Whatman 42 paper, washed three times with distilled water, dried at room temperature, heated at 110 °C for 3 h, and then calcined in air at 500 °C for 8 h. The resulting materials were labeled as Fe_2O_3(0.02)Fe-RH-MCM-41, Fe_2O_3(0.04)Fe-RH-MCM-41, Fe_2O_3(0.06)Fe-RH-MCM-41, Fe_2O_3(0.08)Fe-RH-MCM-41, and Fe_2O_3(0.10)Fe-RH-MCM-41. The Fe-total content in the five samples was determined by the AAS method.

Removing of Fe_2O_3 from Fe_2O_3-Fe-RH-MCM-41

Each 0.5 g of Fe_2O_3-Fe-RH-MCM-41 material acquired from the previous procedure was put into 50 mL of HCl 0.01 M, then magnetically stirred at ambient temperature for 2 h. The sediments were then separated by filtering with Whatman No. 42 paper, washed three times with distilled water, dried at room temperature, and then dried at 110 °C for 2 h. The new

materials were labeled as (0.02)Fe-RH-MCM-41, (0.04)Fe-RH-MCM-41, (0.06)Fe-RH-MCM-41, (0.08)Fe-RH-MCM-41, and (010)Fe-RH-MCM-41. The content of Fe-frameworks in the five samples was determined by the AAS method, while the content of Fe-non-frameworks is the difference between Fe-total and Fe-frameworks.

■ RESULTS AND DISCUSSION

X-ray Diffractogram Analysis

The X-ray diffractograms for RH-MCM-41 and Fe_2O_3-Fe-RH-MCM-41 were collected in Fig. 1(A) (small angle) and 1(B) (wide angle). The standard XRD pattern of α-Fe_2O_3 (ICDD No. 33-0664) is included in Fig. 1(B/g) for comparison. The small angle diffractogram for RH-MCM-41 (Fig. 1(A/a)) exhibits three well-resolved bands that can be indexed as 100, 110, and 200 reflections indicated with 2D p6mm hexagonal symmetry of the lattice. All samples of Fe_2O_3-Fe-RH-MCM-41, which were synthesized with Fe^{3+} concentration of less than 0.1 M (Fig. 1(A/b-e)), still had three diffraction peaks with fairly high intensity. This shows a high degree of pore symmetry even after impregnation. However, the synthesized Fe_2O_3-Fe-RH-MCM-41 sample with a 0.1 M Fe^{3+} concentration (Fig. 1(A/f)) only had two diffraction peaks with relatively low intensity. This is an indication of damage to some of the pore structures [44].

The decrease in intensity of the small angle diffractogram on all samples after the impregnation should be attributed to the incorporation of Fe_2O_3 nanoparticles in the pores. These Fe_2O_3 nanoparticles lessen the contrasting scatter of the mesoporous materials pores and frameworks. Erdem et al. [45] and Costa et al. [46] stated that, in general, the scattering intensity for Bragg reflections decreased when the scattering material

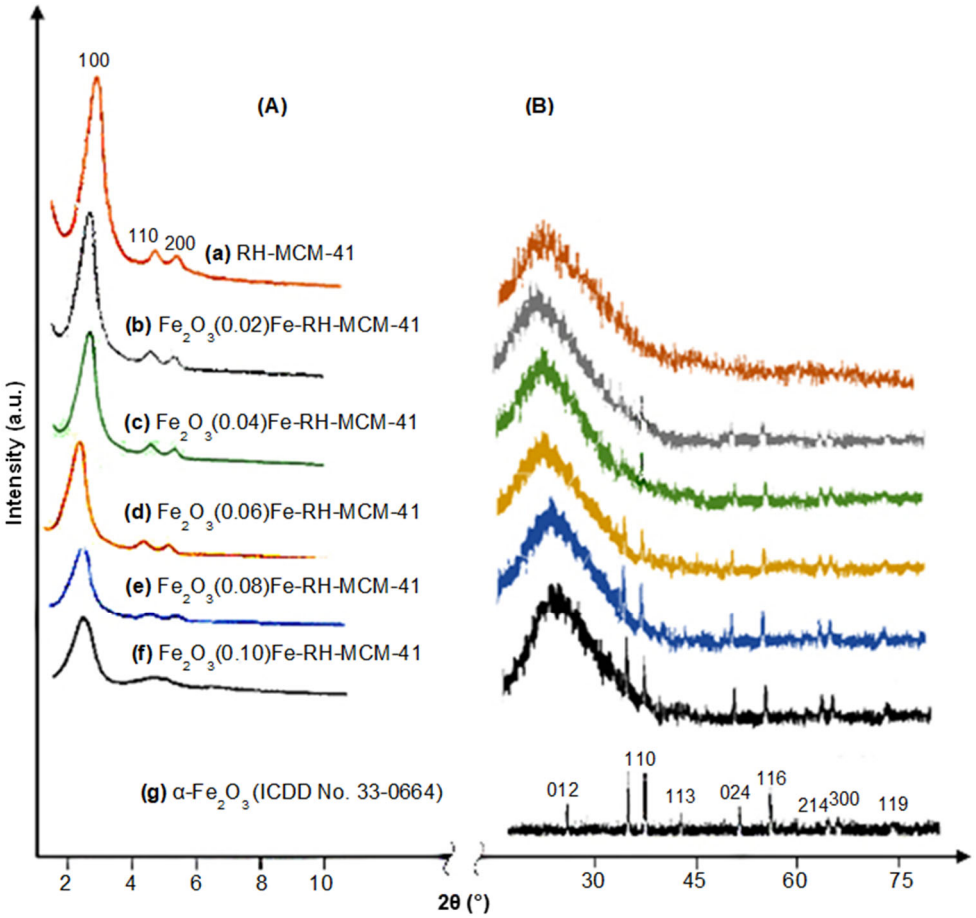

Fig 1. The X-ray diffractogram of RH-MCM-41 and Fe_2O_3-Fe-RH-MCM-41 in the small angle (A) and wide angle (B/a-f), and hematite (B/g)

was filled into the pores because it increased the phase cancellation between the scattering from the walls and the pore region.

The absorption widens with a peak at 2θ = 23° (Fig. 1(B/a-f)), characteristic of the amorphous silica forming the pore walls (ICDD 29-0085). In addition, characteristic weak peaks for hematite (α-Fe_2O_3) were observed at 2θ 30–75° (Fig. 1(B/b-f)), where the intensity increased with increasing Fe^{3+} concentration in the precursor solution. This case also indicates that the impregnation of Fe^{3+} into the pores of MCM-41 resulted in the formation of α-Fe_2O_3 particles outside the frameworks.

As illustrated in Fig. 2, iron oxide nanoparticles developing in RH-MCM-41's pores are thought to be triggered by hydrogen bonds developing between the silanol groups on the RH-MCM-41 surface and the hydrated Fe(III) cations, such as the two-core cation $Fe_2(OH)_2(H_2O)^{4+}$, which is present in large amounts in a pH-low solution of Fe(III) [47]. The concentration of $Fe_2(OH)_2(H_2O)^{4+}$ increased significantly during the filtering, washing, and calcination operations, reaching a super-saturated state and precipitating iron oxide nanoparticles.

The impregnation of Fe^{3+} also induces the reflected diffraction peaks of all samples to shift to a lower diffraction angle (2θ), indicating an increase in both basal spacing (d) and lattice parameter (a_o). The increase in these parameters can be attributed to isomorphic substitution, in which tetravalent silicon in the frameworks is replaced by trivalent iron. This increase occurs because the Pauling radius of Fe (64 pm) is larger than that of Si (42 pm). As a result, the bond length of Fe-O is larger than that of Si-O, and thus the lattice parameters are increased. Similar results have also been reported by previous researchers [48-49].

As illustrated in Fig. 3, it is believed that the isomorphic substitution mechanism of Si^{4+} in the frameworks by Fe^{3+} is initiated by the protonation of the two oxygen atoms of the siloxane bridge (O-Si-O), which causes the breaking of the two Si-O bonds, followed by the release of Si^{4+} and the entry of Fe^{3+}. There is an excess of negative charge on Fe in the product because Si with a charge of 4+ is replaced by Fe with a charge of 3+. The positive ions, primarily H^+, neutralize the negative charge, leading to the formation of Brønsted acid sites, which is very useful for catalytic activity.

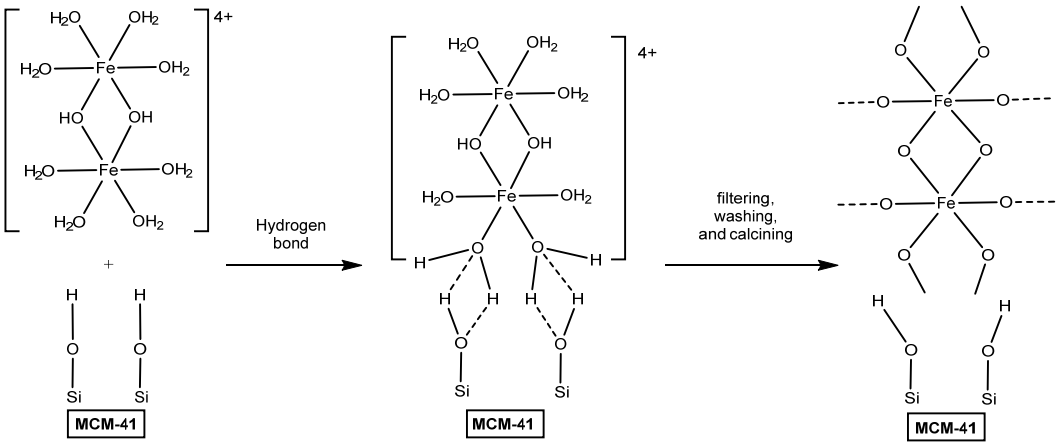

Fig 2. Mechanism estimation of the formation of iron oxide nanoparticles in the pores of RH-MCM-41

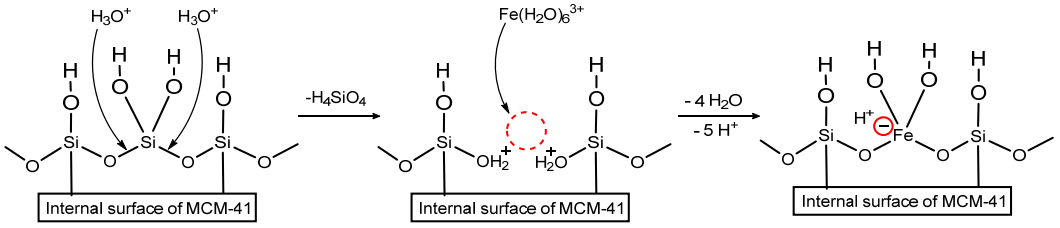

Fig 3. Estimation on the mechanism of isomorphous substitution of Si^{4+} in the MCM-41 frameworks by Fe^{3+}

FTIR Spectra Analysis

Fig. 4 shows the FTIR spectra of RH-MCM-41 and all of Fe_2O_3-Fe-RH-MCM-41. For comparison, the α-Fe_2O_3 (hematite) spectrum is also presented. The absorption of the asymmetric stretching vibration of OH silanol groups and adsorbed water molecules emerged as a widened peak of about 3400 cm^{-1} in all spectra. The peak of about 940 cm^{-1} is due to the symmetric and antisymmetric stretching of Si-O bonds within tetrahedral SiO_4 groups [50]. The symmetrical strain vibration of the Si-O-Si link of the RH-MCM-41 frameworks is represented by the absorption peak of 1084 cm^{-1}, while the bending vibration of the adsorbed water is represented by the absorption peak of 1635 cm^{-1} (remember the hydrophilic property of the OH group). A symmetric Si-O-Si stretching mode is connected with the band near 842 cm^{-1}, whereas a SiO_4 bending mode is associated with the band near 461 cm^{-1} [51].

In Fig. 4(f), Fe-O-Fe vibrations of Fe_2O_3 in the RH-MCM-41 pore cause the weak peaks at 635 and 572 cm^{-1} [52]. The intensity of these two peaks increased along with the increasing concentration of Fe^{3+} in the precursor solution. The absorption at 1084 cm^{-1}, which is typical of the Si-O-Si group's strain vibration, changed to 1076 cm^{-1}. This shows that a part of Si in the framework has been replaced by Fe, resulting in the creation of Si-O-Fe bonds with a higher reduced mass. The band at 461 cm^{-1}, which is associated with SiO_4's bending mode in RH-MCM-41, changed to 438 cm^{-1} due to the bending vibrations of Fe(III)-O-Si in the Fe_2O_3-Fe-RH-MCM-41 frameworks. At around 446 cm^{-1}, another peak linked with Fe-O bonding was found, which was

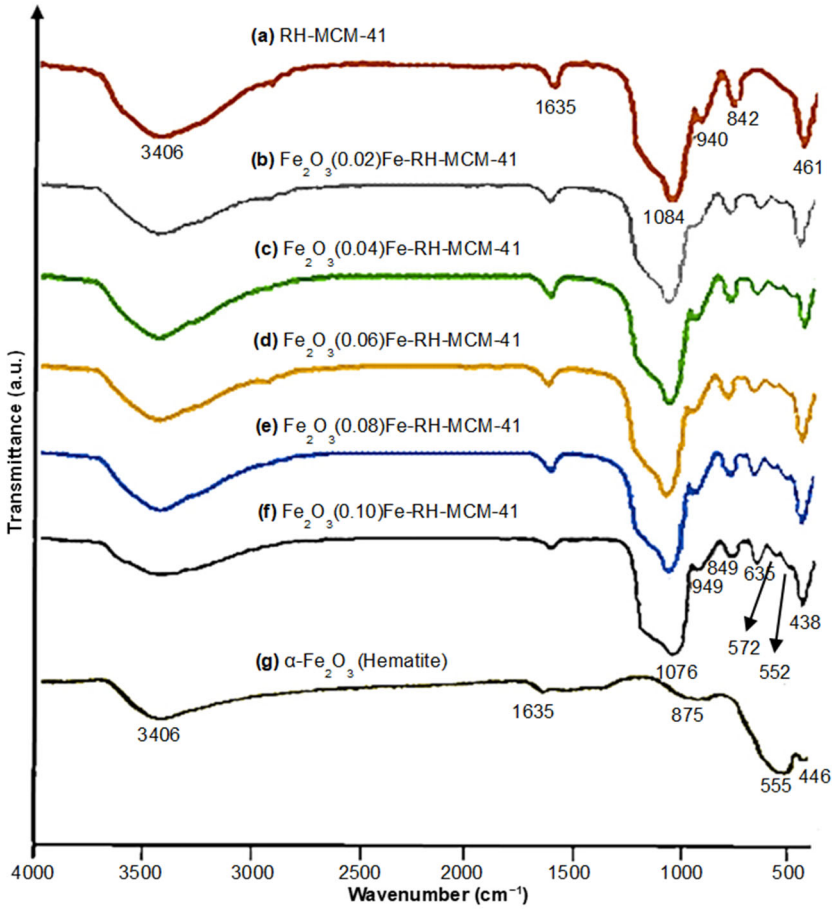

Fig 4. The FTIR Spectra of RH-MCM-41 and Fe-containing RH-MCM-41. The spectrum of α-Fe_2O_3 (hematite) is included for comparison

related to the Fe-O strain mode [53]. This peak, however, coincides with the peak bend vibrations of Fe(III)-O-Si, which are 438 cm^{-1}. Thus, the isomorphic substitution of Si^{4+} on the pore wall by Fe^{3+} and the creation of iron oxide nanoparticles in the pores of RH-MCM-41 are clearly visible in the FTIR spectral analysis. The absence of a nitrate-like peak at 1380 cm^{-1} shows that the iron(III) salt has entirely decomposed.

Gas Sorption Analysis

The N_2 adsorption-desorption isotherms of RH-MCM-41 and Fe-containing RH-MCM-41 are collected in Fig. 5. The isotherm of RH-MCM-41 showed typical IV isotherms, indicating a typical mesoporous material with hexagonal cylindrical channels [54]. The rise in the isotherm curve at low pressure ($P/P_0 < 0.3$) was attributed to the adsorption of a single layer of N_2 on the walls of the pore. The step with a steep slope of about $0.30 < P/P_0 < 0.38$ represents capillary condensation in the pores of RH-MCM-41. The homogeneity of pores and their narrow size distribution is to blame for the acuity of this isotherm's capillary condensation stage. The presence of relatively homogeneous pores with a restricted size distribution accounts for the steep slope of the curve during these isotherms' capillary condensation stage. These findings are consistent with the XRD patterns (Fig. 1(A/a)), which show well-resolved secondary and tertiary diffraction above 2θ = 4–6° ([110] and [200] peaks) and indicate a very long-range order of these materials. The H1-type hysteresis loop in this range is caused by the capillary condensation that is typical for mesoporous materials. The almost flat curve at the end was attributed to the multilayer adsorption on the surface of mesopores. The H4-type hysteresis loop that appears at $P/P_0 > 0.40$ indicates the narrow pore size distribution contained in the material.

The isotherms of Fe_2O_3-(0.02)-Fe-RH-MCM-41, Fe_2O_3-(0.04)-Fe-RH-MCM-41, and Fe_2O_3-(0.06)-Fe-RH-MCM-41, which were of type IV and almost identical to the parent RH-MCM-41, indicated that the pore dimension of the host materials still remained. This case shows that the resulting Fe_2O_3-Fe-MCM-41 material still has a mesoporous structure, and iron oxide nanoparticles only fill a small part of the RH-MCM-41 pores. However,

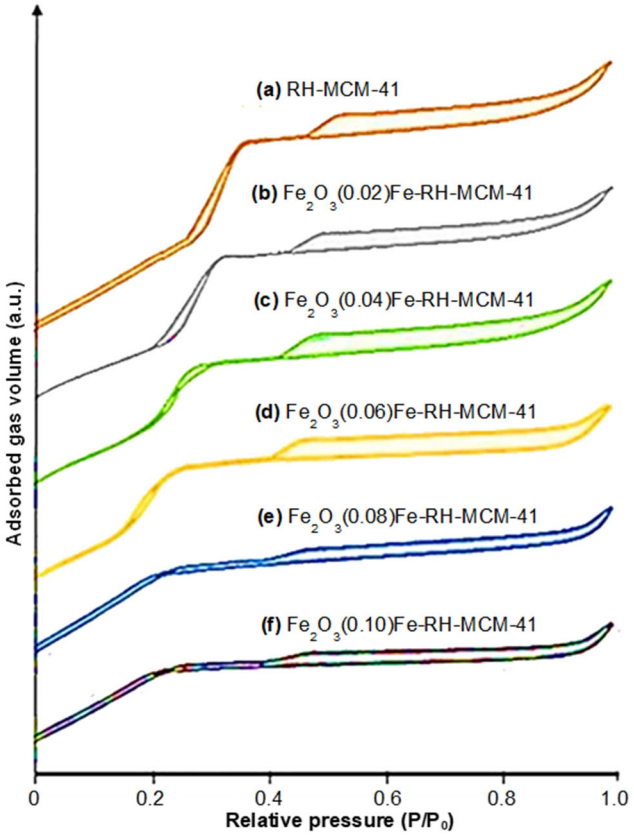

Fig 5. The N_2 adsorption-desorption isotherms of RH-MCM-41 and Fe_2O_3-Fe-RH-MCM-41

the starting point of the inflection shifts further left (toward a smaller P/P_0), which marks the reduction of pore size. Additionally, the height of the curve reduces, which indicates a reduced specific surface area. This was caused by the increasing amount of material (iron oxide) that filled the mesoporous channels as a result of the greater concentration of Fe^{3+} in the precursor solution.

In contrast, samples of Fe_2O_3-(0.08)-Fe-RH-MCM-41 and Fe_2O_3-(0.10)-Fe-RH-MCM-41 showed an isotherm that is markedly different from the parent RH-MCM-41 silica. The characteristic pore-filling step of the isotherm disappears for the two samples. This feature is thought to be due to the significant narrowing of the RH-MCM-41 pore, as it is partially blocked by iron oxide particles [55]. According to this explanation, Table 1 shows a systematic decrease in surface area, specific pore volume, and pore diameter as the impregnated Fe^{3+} concentration increases, where a significant decrease occurs in the fifth and sixth samples.

Analysis of TEM

The TEM images of RH-MCM-41 and Fe_2O_3-(0.06)-Fe-RH-MCM-41 samples are presented in Fig. 6. The TEM image of the RH-MCM-41 sample (Fig. 6(a)) shows that the pores are regularly arranged in a hexagonal shape, related to the p6mm 2D hexagonal symmetry. This is in agreement with the analytical results of the XRD data. In addition, Fig. 6(a) reveals a significant degree of pore regularity with a pore diameter of 2.9 nm. For Fe_2O_3-(0.06)-Fe-RH-MCM-41 (Fig. 6(b)), TEM images show a pore diameter of 2.5 nm. This is also close to the results obtained from GSA data, which are 2.861 nm. This result matches those found by GSA data, showing that the average pore diameter of this material was 3.241 nm.

The decrease in pore diameter can be attributed to the presence of iron oxide nanoparticles, which form and fill some of the pores. In addition, Fig. 6(b) also shows the reduced pore regularity caused by the isomorphic substitution of Si^{4+} by Fe^{3+} that occurs in the frameworks, indicated by the shift of the 100-plane peak to the left side, as discussed previously.

Table 1. The porosity of RH-MCM-41 and Fe_2O_3-Fe-RH-MCM-41 samples

Sample	S_{BET}[(a)] (m^2/g)	V_P[(b)] (mL/g)	D_{BJH}[(c)] (nm)
RH-MCM-41	934	0.759	3.241
Fe_2O_3-(0.02)-Fe-RH-MCM-41	916	0.703	3.088
Fe_2O_3-(0.04)-Fe-RH-MCM-41	897	0.668	2.965
Fe_2O_3-(0.06)-Fe-RH-MCM-41	886	0.632	2.861
Fe_2O_3-(0.08)-Fe-RH-MCM-41	567	0.421	2.398
Fe_2O_3-(0.10)-Fe-RH-MCM-41	432	0.398	2.013

Note: (a) Using adsorption data with a P/P0 range of 0.05 to 0.30, the multipoint BET technique was used to determine BET surface area; (b) The specific pore volume is calculated using P/P0 = 0.95; (c) The BJH approach was used to determine the sizes of the pores from the nitrogen isotherm's adsorption branch

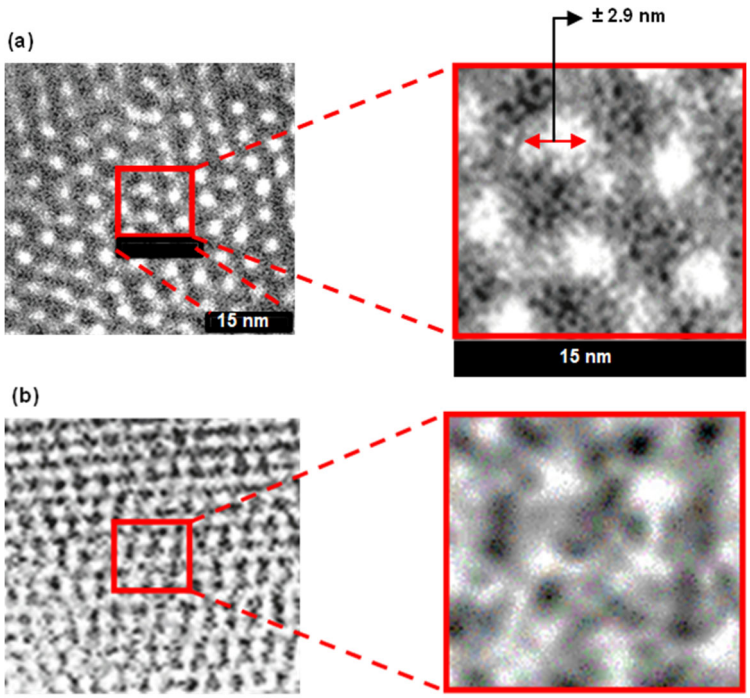

Fig 6. The TEM image of RH-MCM-41 and Fe_2O_3-(0.06)-Fe-RH-MCM-41 sample

The Content of Fe

The interpretation of the XRD diffractogram indicated that the Fe^{3+} impregnation of the MCM-41 pores led to the isomorphous substitution of Si^{4+} by Fe^{3+} as well as the formation of iron oxide at the out of frameworks. Table 2 shows the Fe content in the materials before and after the HCl treatment. The content of Fe increases with the increase in Fe^{3+} concentration in the precursor solution. The maximum Fe^{3+} concentration that can be used without causing damage to the pore structure of RH-MCM-41 is 0.08 M, which produces a material with a Fe content of 2.97%. Several researchers have previously reported comparable Fe contents. He et al. [56] reported a maximum Fe content of 1% by weight in Fe-MCM-41 material produced in situ without harming the silica host. Pasqua et al. [57] modified the process to manage the incorporation of Fe to the point where the content reaches 5% by weight without harming the silica host.

As shown in Table 2, the treatment using a solution of 0.01 M HCl caused a decrease in the amount of Fe content. The reaction associated with the decrease in Fe content is [58]:

$$Fe_2O_{3(s)} + 6HCl_{(aq)} \rightarrow 2FeCl_{3(aq)} + 3H_2O_{(l)}$$

In this case, Fe_2O_3 was iron oxide particles dispersed on the outer surface of the silica frameworks, both inside and outside of the pores (denoted as Fe-non-frameworks). The HCl treatment was assumed to dissolve all of the Fe-non-frameworks but not for Fe isomorphic substituted in the frameworks (denoted as Fe-frameworks). Based on this assumption, the composition of Fe in the initial sample (before treatment) can be deduced, as shown in Table 3.

By using the bar curve (Fig. 7), the difference in Fe content between Fe-frameworks and Fe-non-frameworks of each sample can be clearly seen. The content of Fe-frameworks in the five samples is almost the same, while that of Fe-non-frameworks is significantly increased when a higher concentration of Fe^{3+} in the precursor solution is used. This trend indicates that Fe-framework content reaches its maximum faster than Fe-non-framework content. Therefore, when a precursor with a higher concentration of Fe^{3+} is used, only a small amount of Fe^{3+} displaces Si^{4+} in the frameworks, whereas most of them form iron oxide particles outside the frameworks. This is not surprising because, based on our calculations, the isomorphic substitution of Si^{4+} by Fe^{3+} in the silica frameworks is endothermic ($\Delta H = +1{,}650$ kJ mol^{-1}), while the formation of Fe_2O_3 outside the frameworks is exothermic ($\Delta H = -16{,}484$ kJ mol^{-1}).

Table 2. The content of Fe in the sample before and after the HCl treatment

Sample	Fe content (wt.%)	
	Before HCl treatment	After HCl treatment
MCM-41	0	0
Fe_2O_3(0.02)Fe-RH-MCM-41	1.12	0.48
Fe_2O_3(0.04)Fe-RH-MCM-41	1.89	0.73
Fe_2O_3(0.06)Fe-RH-MCM-41	2.53	0.86
Fe_2O_3(0.08)Fe-RH-MCM-41	2.97	0.89
Fe_2O_3(0.10)Fe-RH-MCM-41	3.19	0.91

Table 3. Composition of Fe in samples before treatment with 0.01 M HCl

Sample	Fe total (wt.%)	Fe-frameworks (wt.%)	Fe-non-frameworks (wt.%)
RH-MCM-41	0	0	0
Fe_2O_3(0.02)Fe-RH-MCM-41	1.12	0.48	0.64
Fe_2O_3(0.04)Fe-RH-MCM-41	1.89	0.73	1.16
Fe_2O_3(0.06)Fe-RH-MCM-41	2.53	0.86	1.67
Fe_2O_3(0.08)Fe-RH-MCM-41	2.97	0.89	2.08
Fe_2O_3(0.10)Fe-RH-MCM-41	3.19	0.91	2.28

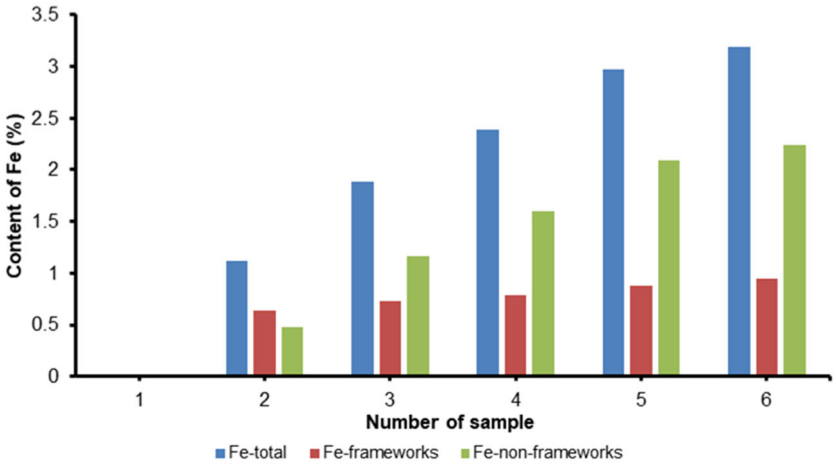

Fig 7. Content of Fe in the samples before treatment with 0.01 M HCl

■ CONCLUSION

According to XRD patterns, N_2 adsorption-desorption isotherms, and a TEM image, rice husk silica can be employed as the starting material for the sonication synthesis of RH-MCM-41, which displays a p6mm hexagonal mesostructure with a high specific surface area and narrow porosity size distribution. Impregnation of Fe^{3+} (0.02, 0.04, 0.06, 0.08, and 0.10 M) into the pores of RH-MCM-41 resulted in iron oxide outside the frameworks as well as isomorphic substitution in the frameworks, in which Fe^{3+} replaced Si^{4+}. The tendency of iron oxide formation is greater than the isomorphic substitution, as shown by the weight percents of Fe-non-frameworks of 0.64, 1.16, 1.67, 2.08, and 2.28% for each sample and the weight percents of Fe-frameworks of 0.48, 0.73, 0.86, 0.89, and 0.91% for each sample. This is due to the fact that isomorphic substitution of Si^{4+} by Fe^{3+} in the silica frameworks is endothermic ($\Delta H = +1{,}650$ kJ mol^{-1}), while the formation of Fe_2O_3 outside the frameworks is exothermic ($\Delta H = -16{,}484$ kJ mol^{-1}). Based on these findings, the mass percentage of Fe-non-frameworks to Fe-frameworks in RH-MCM-41 can be controlled by adjusting the concentration of Fe^{3+} used in the impregnation process. This is very important if the material is going to be applied as a catalyst, because the presence of iron oxide nanoparticles to a certain degree can increase the catalytic activity, but in contrast, excessive addition may also block the active site of Brønsted acid and therefore reduce the catalytic activity.

■ ACKNOWLEDGMENTS

The authors acknowledge financial support from a research grant administered by Universitas Gadjah Mada under the funding contract number 0127/J01.1.28/PL.06.02/2015 from the Directorate General of Higher Education (DGHE), Ministry of Education, Culture, Research, and Technology, The Republic of Indonesia.

■ REFERENCES

[1] Li, S.C., Lin, Y.C., and Li, Y.P., 2021, Understanding the catalytic activity of microporous and mesoporous zeolites in cracking by experiments and simulations, *Catalysts*, 11 (9), 1114.

[2] Ho, P.H., Yao, D., Creaser, D., and Olsson, L., 2022, Advantages of high-siliceous zeolites in the reactivity and stability of diesel oxidation catalysts, *ACS Eng. Au*, 2 (3), 219–235.

[3] Bingre, R., Louis, B., and Nguyen, P., 2018, An overview on zeolite shaping technology and solutions to overcome diffusion limitations, *Catalysts*, 8 (4), 163.

[4] Costa, J.A.S, de Jesus, R.A., Santos, D.O., Mano, J.F., Romão, L.P.C., and Paranhos, C.M., 2020, Recent progresses in the adsorption of organic, inorganic, and gas compounds by MCM-41-based mesoporous materials, *Microporous Mesoporous Mater.*, 291, 109698.

[5] Dinh Du, P., Hieu, N.T., To, T.C., Bach, L.G., Tinh, M.X., Mau, T.X., and Quang Khieu, D., 2019,

Aminopropyl functionalised MCM-41: Synthesis and application for adsorption of Pb(II) and Cd(II), *Adv. Mater. Sci. Eng.*, 2019, 8573451.

[6] Valiey, E., Dekamin, M.G., and Alirezvani, Z., 2021, Sulfamic acid pyromellitic diamide-functionalized MCM-41 as a multifunctional hybrid catalyst for melting-assisted solvent-free synthesis of bioactive 3,4-dihydropyrimidin-2-(1*H*)-ones, *Sci. Rep.*, 11 (1), 11199.

[7] Oliveira, D.M., and Andrada, A.S., 2019, Synthesis of ordered mesoporous silica MCM-41 with controlled morphology for potential application in controlled drug delivery systems, *Cerâmica*, 65 (374), 170–179.

[8] Ng, E.P., Goh, J.Y., Ling, T.C., and Mukti, R.R., 2013, Eco-friendly synthesis for MCM-41 nanoporous materials using the non-reacted reagents in mother liquor, *Nanoscale Res. Lett.*, 8 (1), 120.

[9] Parangi, T.F., Patel, R.M., and Chudasama, U.V., 2014, Synthesis and characterization of mesoporous Si-MCM-41 materials and their application as solid acid catalysts in some esterification reactions, *Bull. Mater. Sci.*, 37 (3), 609–615.

[10] Juárez-Serrano, N., Berenguer, D., Martínez-Castellanos, I., Blasco, I., Beltrán, M., and Marcilla, A., 2021, Effect of reaction time and hydrothermal treatment time on the textural properties of SBA-15 synthesized using sodium silicate as silica source and its efficiency for reducing tobacco smoke toxicity, *Catalysts*, 11 (7), 808.

[11] Fu, P., Yang, T., Feng, J., and Yang, H., 2015, Synthesis of mesoporous silica MCM-41 using sodium silicate derived from copper ore tailings with an alkaline molted-salt method, *J. Ind. Eng. Chem.*, 29, 338–343.

[12] Yang, G., Deng, Y., Ding, H., Lin, Z., Shao, Y., and Wang, Y., 2015, A facile approach to synthesize MCM-41 mesoporous materials from iron ore tailing: Influence of the synthesis conditions on the structural properties, *Appl. Clay Sci.*, 111, 61–66.

[13] Yang, G., Deng, Y., and Wang, J., 2014, Non-hydrothermal synthesis and characterization of MCM-41 mesoporous materials from iron ore tailing, *Ceram. Int.*, 40 (5), 7401–7406.

[14] Shah, B.A., Patel, A.V., Bagia, M.I., and Shah, A.V., 2017, Green approach towards the synthesis of MCM-41 from siliceous sugar industry waste, *Int. J. Appl. Chem.*, 13 (3), 497–514.

[15] Lin, Y.W., Lee, W.H., Lin, K.L., and Kuo, B.Y., 2021, Synthesis and grafted NH_2-Al/MCM-41 with amine functional groups as humidity control material from silicon carbide sludge and granite sludge, *Processes*, 9 (12), 2107.

[16] Ali-Dahmane, T., Brahmi, L., Hamacha, R., Villieras, F., and Bengueddach, A., 2016, Synthesis of MCM-41 nanomaterial from Algerian bentonite: Influence of synthesis pH, *J. Fundam. Appl. Sci.*, 9 (2), 636–649.

[17] Zhang, X., and Du, T., 2022, Study of rice husk ash derived MCM-41-type materials on pore expansion, Al incorporation, PEI impregnation, and CO_2 adsorption, *Korean J. Chem. Eng.*, 39 (3), 736–759.

[18] Abbas, S.H., Adam, F., and Muniandy, L., 2020, Green synthesis of MCM-41 from rice husk and its functionalization with nickel(II) salen complex for the rapid catalytic oxidation of benzyl alcohol, *Microporous Mesoporous Mater.*, 305, 110192.

[19] Suyanta, S., and Kuncaka, A., 2011, Utilization of rice husk as raw material in synthesis of mesoporous silicates MCM-41, *Indones. J. Chem.*, 11 (3), 279–284.

[20] Nguyen, T.T., Ma, H.T., Avti, P., Bashir, M.J.K., Ng, C.A., Wong, L.Y., Jun, H.K., Ngo, Q.M., and Tran, N.Q., 2019, Adsorptive removal of iron using SiO_2 nanoparticles extracted from rice husk ash, *J. Anal. Methods Chem.*, 2019, 6210240.

[21] Jongpradist, P., Homtragoon, W., Sukkarak, R., Kongkitkul, W., and Jamsawang, P., 2018, Efficiency of rice husk ash as cementitious material in high-strength cement-admixed clay, *Adv. Civ. Eng.*, 2018, 8346319.

[22] Xu, K., Sun, Q., Guo, Y., and Dong, S., 2013, Effects on modifiers on the hydrophobicity of SiO_2 films from nano-husk ash, *Appl. Surf. Sci.*, 276, 796–801.

[23] Nguyen, M.N., 2020, Worldwide bans of rice straw burning could increase human arsenic exposure, *Environ. Sci. Technol.*, 54 (7), 3728–3729.

[24] Cazula, B.B., Oliveira, L.G., Machado, B., and Alves, H.J., 2021, Optimization of experimental conditions for the synthesis of Si-MCM-41 molecular sieves using different methods and silica sources, *Mater. Chem. Phys.*, 266, 124553.

[25] Meléndez-Ortiz, H.I., Mercado-Silva, A., García-Cerda, L.A., Castruita, G., and Perera-Mercado, Y.A., 2013, Hydrothermal synthesis of mesoporous silica MCM-41 using commercial sodium silicate, *J. Mex. Chem. Soc.*, 57 (2), 73–79.

[26] Golezani, A.S., Fateh, A.S., and Mehrabi, H.A., 2016, Synthesis and characterization of silica mesoporous material produced by hydrothermal continues pH adjusting path way, *Prog. Nat. Sci.: Mater. Int.*, 26 (4), 411–414.

[27] Santos, E.C., Costa, L.S., Oliveira, E.S., Bessa, R.A., Freitas, A.D.L., Oliveira, C.P., Nascimento, R.F., and Loiola, A.R., 2018, Al-MCM-41 synthesized from kaolin via hydrothermal route: Structural characterization and use as an efficient adsorbent of methylene blue, *J. Braz. Chem. Soc.*, 29 (11), 2378–2386.

[28] Deka, J.R., Vetrivel, S., Wu, H.Y., Pan, Y.C., Ting, C.C., Tsai, Y.L., and Kao, H.M., 2014, Rapid sonochemical synthesis of MCM-41 type benzene-bridged periodic mesoporous organosilicas, *Ultrason. Sonochem.*, 21 (1), 387–394.

[29] Sönmez, D.M., Gudovan, D., Truşca, R. Ficai, D., Andronescu, E., and Vasile, B.S., 2015, Synthesis, characterization and testing of MCM-41/TiO_2 catalyst for organic dye degradation, *Dig. J. Nanomater. Biostruct.*, 10 (4), 1329–1341.

[30] Soltani, R., Dinari, M., and Mohammadnezhad, G., 2018, Ultrasonic-assisted synthesis of novel nanocomposite of poly (vinyl alcohol) and amino-modified MCM-41: A green adsorbent for Cd(II) removal, *Ultrason. Sonochem.*, 40, 533–542.

[31] Wang, X., Chen, W., Zhou, M., Zhang, Z., and Zhang, L., 2022, Dynamics of double bubbles under the driving of burst ultrasound, *Ultrason. Sonochem.*, 84, 105952.

[32] Yu, X., and Williams, C.T., 2022, Recent advances in the applications of mesoporous silica in heterogeneous catalysis, *Catal. Sci. Technol.*, 12 (19), 5765–5794.

[33] Srividhya, N., 2014, Synthesis characterization and catalytic evaluation of mesoporous Fe-MCM-41 and Si-MCM-41 materials, *IOSR J. Appl. Chem.*, 7 (6), 41–49.

[34] Zhang, Q., Wang, Y., Itsuki, S., Shishido, T., and Takehira, K., 2001, Fe-MCM-41 for selective epoxidation of styrene with hydrogen peroxide, *Chem. Lett.*, 30 (9), 946–947.

[35] Dhal, J.P., Dash, T., and Hota, G., 2020, Iron oxide impregnated mesoporous MCM-41: Synthesis, characterization and adsorption studies, *J. Porous Mater.*, 27 (1), 205–216.

[36] Mokhonoana, M.P., and Coville, N.J., 2009, Highly loaded Fe-MCM-41 materials: Synthesis and reducibility studies, *Materials*, 2 (4), 2337–2359.

[37] Sasieekhumar, A.R., Somanathan, T., Abilarasu, A., and Shanmugam, M., 2017, Mesoporous Fe/MCM-41 as heterogeneous photocatalyst for the photodegradation of methylene blue, *Res. J. Pharm. Technol.*, 10 (10), 3398–3400.

[38] Guo, Y., Chen, B., Zhao, Y., and Yang, T., 2021, Fabrication of the magnetic mesoporous silica Fe-MCM-41-A as efficient adsorbent: Performance, kinetics and mechanism, *Sci. Rep.*, 11 (1), 2612.

[39] Huo, C., Ouyang, J., and Yang, H., 2014, CuO nanoparticles encapsulated inside Al-MCM-41 mesoporous materials via direct synthetic route, *Sci. Rep.*, 4 (1), 3682.

[40] Yang, G., Xu, Y., Su, X., Xie, Y., Yang, C., Dong, Z., and Wang, J., 2014, MCM-41 supported CuO/Bi_2O_3 nanoparticles as potential catalyst for 1,4-butynediol synthesis, *Ceram. Int.*, 40 (3), 3969–3973.

[41] Li, X., Liu, W., Ma, J., Wen, Y., and Wu, Z., 2015, High catalytic activity of magnetic FeO_x/NiO_y/SBA-15: The role of Ni in the bimetallic oxides at the nanometer level, *Appl. Catal., B*, 179, 239–248.

[42] Hassanzadeh-Afruzi, F., Asgharnasl, S., Mehraeen, S. Amiri-Khamakani, Z., and Maleki, A., 2021, Guanidinylated SBA-15/Fe_3O_4 mesoporous nanocomposite as an efficient catalyst for the

synthesis of pyranopyrazole derivatives, *Sci. Rep.*, 11 (1), 19852.

[43] Pieterse, J.A.Z., Booneveld, S., and van den Brink, R.W., 2005, Evaluation of Fe-zeolite catalysts prepared by different methods for the decomposition of N_2O, *Appl. Catal., B*, 45, 156–172.

[44] Atchudan, R., Perumal, S., Jebakumar Immanuel Edison, T.N., and Lee, Y.R., 2015, Highly graphitic carbon nanosheets synthesized over tailored mesoporous molecular sieves using acetylene by chemical vapor deposition method, *RSC Adv.*, 5 (113), 93364–93373.

[45] Erdem, S., Erdem, B., Öksüzoglu, R.M., and Çitak, A., 2013, Bifunctional Fe-SBA-15-SO_3H mesoporous catalysts with different Si/Fe molar ratios: Synthesis, characterization and catalytic activity, *Bull. Korean Chem. Soc.*, 34 (5), 1481–1486.

[46] Costa, M.B.G., Juárez, J.M., and Anunziata, O.A., 2016, "Synthesis and Characterization of CMK Porous Carbons Modified with Metals Applied to Hydrogen Uptake and Storage" in *Microporous and Mesoporous Materials*, Eds. Dariani, R.S., IntechOpen, Rijeka, Croatia, 51–85

[47] Cotton, F.A., and Wilkinson, G., 1976, *Basic Inorganic Chemistry*, Wiley, New York, US.

[48] Qian, W., Wang, H., Chen, J., and Kong, Y., 2015, Spherical V-Fe-MCM-48: The synthesis, characterization and hydrothermal stability, *Materials*, 8 (4), 1752–1765.

[49] AlDhawi, Z.A., Alomair, N.A., Kochkar, H., and Grevathy, C.G., 2022, One pot synthesis of chromium incorporated SBA-16 under acid medium-application in the selective oxidation of benzyl alcohol derivatives, *Arabian J. Chem.*, 15 (7), 103861.

[50] Yusuf, M.O., 2023, Bond characterization in cementitious material binders using Fourier-transform infrared spectroscopy, *Appl. Sci.*, 13 (5), 3353.

[51] Casillas, P.E.G., Pérez, C.A.M., Gonzalez, C.A.R., 2012, "Infrared Spectroscopy of Functionalized Magnetic Nanoparticles" in *Infrared Spectroscopy - Materials Science, Engineering and Technology*, Eds. Theophanides, T., IntechOpen, Rijeka, Croatia, 405–420.

[52] Ulu, A., Noma, S., Koytepe, S., and Ates, B., 2018, Magnetic Fe_3O_4@MCM-41 core–shell nanoparticles functionalized with thiol silane for efficient L-asparaginase immobilization, *Artif. Cells, Nanomed., Biotechnol.*, 46, 1035–1045.

[53] Quy, D.V., Hieu, N.M., Tra, P.T., Nam, N.H., Hai, N.H., Thai Son, N., Nghia, P.T., Anh, N.T.V., Hong, T.T., and Luong, N.H., 2013, Synthesis of silica-coated magnetic nanoparticles and application in the detection of pathogenic viruses, *J. Nanomater.*, 2013, 603940.

[54] Sing, K.S.W., Everett, D.H., Haul., R.A.W., Moscou, L., Pierotti, R.A., Rouquérol, J., and Siemieniewska, T., 1985, Reporting physisorption data for gas/solid systems with special reference to the determination of surface area and porosity, *Pure Appl. Chem.*, 57 (4), 603–619.

[55] Huang, S., Fan, Y., Cheng, Z., Kong, D., Yang, P., Quan, Z., Zhang, C., and Lin, J., 2009, Magnetic mesoporous silica spheres for drug targeting and controlled release, *J. Phys. Chem. C*, 113 (5), 1775–1784.

[56] He, N.Y., Cao, J.M., Bao, S.L., and Xu, Q.H., 1997, Room-temperature synthesis of an Fe-containing mesoporous molecular sieve, *Mater. Lett.*, 31 (1-2), 133–136.

[57] Pasqua, L., Testa, F., Aiello, R., Di Renzo, F., and Fajula, F., 2001, Influence of pH and nature of the anion on the synthesis of pure and iron-containing mesoporous silica, *Microporous Mesoporous Mater.*, 44-45, 111–117.

[58] Chastukhin, A.E., Izotov, A.D., Gorichev, I.G., and Kutepov, A.M., 2004, Analysis of the kinetics of iron(II, III) oxide dissolution in hydrochloric acid using a generalized Delmon Model, *Theor. Found. Chem. Eng.*, 38 (1), 81–85.